NANO EXPRESS   **Open Access**

Check for updates

Sn$_x$P$_y$ Monolayers: a New Type of Two-Dimensional Materials with High Stability, Carrier Mobility, and Magnetic Properties

Yan-Mei Dou, Chang-Wen Zhang, Ping Li and Pei-Ji Wang[*]

Abstract

Searching for two-dimensional (2D) group V materials with ferromagnetism, elastic anisotropy, and carrier mobility and tunable band structure is one key to developing constantly developing nanodevices. The 2D monolayers Sn$_x$P$_y$ with x/y (1/1, 1/2, 1/3, and so on) coordination number are studied based on the particle-swarm optimization technique combined with the density functional theory optimization. Its thermal stability can be confirmed by molecular dynamics at 70K and 300K, indicating that the novel 2D materials have a stable existence. The electronic band structures of four stable structures suggest that all the monolayers of Sn$_x$P$_y$ are fully adjustable and flexible tunable band gaps semiconductors under the biaxial strain. The monolayer of P$\bar{4}2_1$m-SnP$_2$ with unique valence band structure can go from nonmagnetic to ferromagnetic by the hole doping because of the "Stoner criterion," and Pmc2$_1$-SnP$_2$ is a direct-like gap semiconductor with in-plane elastic anisotropy to possess a high electron mobility as high as 800 cm^{2}V^{-1} s^{-1} along the k_b direction, which is much higher than that of MoS$_2$ ($\sim$ 200 cm^{2}V^{-1} s^{-1}). The optical absorption peak of the material is in the ultraviolet region. These discoveries expand the potential applications of the emerging field of 2D Sn$_x$P$_y$ structures in nanoelectronics.

Keywords: Sn$_x$P$_y$, Monolayers, Carrier mobility, Magnetic properties, Optical property

Introduction

Two-dimensional (2D) binary compounds have attracted extensive attention in recent years due to their unique properties and can provide reliable guidance for its potential applications in nanoelectronics and optoelectronic devices [1]. For instance, graphene attracted great interest since its discovery due to properties and potential applications [2–6], whereas graphene has undetectable small band gap at room temperature, making it difficult to use in optoelectronic nanodevices. So, these difficulties promoted researchers to resolve to find 2D materials with an ideal band gap. In the following years, boron-nitride (BN) [7], MoS$_2$ or other transition metal dichalcogenides [8–13], and transition-metal trichalcoge-nides [14, 15], among others are coming out. In recent years, graphene and other 2D materials of the group IV (silicone, stanene, and germanene [16]) have made good progress in scientific research. Except, 2D semiconductor materials belonging to the group V, especially phosphorene [17–19] and arsenene [20], are emerging as a new generation of contenders in the field of optoelectronic devices. Phosphene has broad application prospects in field-effect transistors, optoelectronic devices, spintronics, gas sensors and solar cells, and so on, while stanene, a 2D honeycomb-like structure, is considered to a new type of material with superior physical properties after graphene due to its strong electron spin-orbit coupling.

It is urgent to synthesize two kinds of elements to get multifunctional novel 2D materials. It is reported that alloying is often used to improve the properties of 2D materials to expand its applicability. For example, 2D MoS$_{2x}$Se$_{2(1-x)}$ and WS$_{2x}$Se$_{2(1-x)}$ nanosheets [21, 22] witness weird properties as tunable electronic, optical properties, and in-plane Negative Poisson's Ratio with $x/$

* Correspondence: ss_wangpj@ujn.edu.cn
School of Physics and Technology, University of Jinan, Jinan 250022, Shandong, People's Republic of China

Dou *et al. Nanoscale Research Letters* (2020) 15:155

Page 2 of 8

y (1/1, 1/2, 1/3, and so on) coordination number. For another example, 2D alloy material Si_xC_y [23], B_xC_y [24], and B_xSi_y [25] show many novel characteristics (newfangled structure, electronic, and mechanical properties) by the first-principles calculation which are different from those of pure ground state. Because 2D phosphorene and stanene monolayers have novel properties, Sn and P elements were be compound with various stoichiometries.

In this work, we built few structures by the particle swarm optimization (PSO) algorithm. Then, we singled out the four most stable structures of 2D Sn_xP_y monolayers with different coordination numbers and investigated the electronic properties on the basis of density functional theory (DFT) optimization. The calculated electronic band structures suggest that all the stable or metastable monolayers with different coordination numbers are semiconductors with an indirect band gap. More importantly, the $Pmc2_1$-SnP_2 monolayer is a direct-like gap semiconductor with a finite band gap of 0.92 eV in the infrared-light region. But beyond that, the $Pmc2_1$-SnP_2 structure is a direct-like gap semiconductor that possesses high electron mobility of ~ 800 $cm^2V^{-1}s^{-1}$, which is much higher than that of MoS_2 (~ 200 $cm^2V^{-1}s^{-1}$). The monolayer of P $\overline{4}2_1$ m-SnP_2 structure with a unique valence band structure can go from nonmagnetic to ferromagnetic by the hole doping because of the "Stoner criterion." The calculated electronic band structures suggest that all the monolayers of Sn_xP_y are semiconductors with flexibly tunable band gaps under the biaxial strain, permitting strain engineering of four structures band gaps within nearly the whole visible-light range.

Computational Methods

In order to guarantee a thorough search of the structural diversity, various *x* and *y* selecting from one to six are taken into account on the basis of the particle-swarm optimization (PSO) algorithm [26]. Results of the search delivered the monolayer structures are relatively steadily only for $y/x \geqq 1$.

To study the electronic structure of 2D Sn_xP_y monolayers with different coordination number, our calculations were performed by using the plane-wave density functional theory (DFT) [27, 28] method to realize in the Vienna Ab-initio Simulation Package (VASP) [29–31]. Through the Generalized Gradient Approximation (GGA) to describe the exchange-correlation energy in the form of Per-dew–Burke–Ernzerhof (PBE) [32–35] and the electron-ion potential is described by the projection amplification wave method [33]. The cutoff energy of the plane-wave was chosen to be 500 eV energy for Sn_xP_y

systems, respectively. A sufficiently dense k point (9 × 9 × 1) of the reciprocal space was sampled in the Brillouin zone. The vacuum space perpendicular to the plane between neighboring super-cells is greater than 25 Å, eliminating the interaction between replications. In the two consecutive steps calculation, it is set as 10^5 eV as the energy convergence value. During the geometric optimization, the atomic forces of all structures are less than 0.02 eV $Å^{-1}$ by using the conjugate gradient method until the atoms reach their optimal position. In addition, we will use the super-cell with 4 × 4 × 1 for ab initio molecular dynamic (AIMD) calculation when the Nosé algorithm [36] at 300K.

Carrier mobility is mainly affected by acoustic side wave scattering, optical side wave scattering, and ionized impurity scattering. Since the latter two are not as influential as the first one, the mobility we calculated includes the mobility under acoustic side wave scattering. Mobility mainly affects two performances of transistors: One is that the carrier concentration together determines the conductivity (the inverse of the resistivity) of the semiconductor material. Second, it affects the working frequency of the device. The main limitation of the frequency response characteristics of bipolar transistors is the time for minority carriers to cross the base region. Mobility is an important parameter to measure the conductivity of 2D semiconductor materials. It determines the conductivity of semiconductor materials and affects the working speed of devices. Thus, carrier mobility is controlled by phonon dispersion and can be described by the deformation potential (DP) theory which is proposed by Bardeen and Shockley [37]. So, the carrier mobility in 2D materials can be expressed as [38, 39]

$$\mu_{2D} = \frac{2e\hbar^3 C^{2D}}{3k_BT|m^*|^2 E_1^2}$$

where e, $\hbar$, and k_B are the electron charge reduced Planck and Boltzmann's constant, respectively. And T is the temperature which set to 300K. Where m^* is the effective mass, E_1 is deformation potential constant, and C^{2D} is the in-plane stiffness.

The linear effect of the system on the light field under the small wave vector is determined by the imaginary part of the complex dielectric constant and the dielectric function which can be calculated by

$$\varepsilon(\omega) = \varepsilon_1(\omega) + i\varepsilon_2(\omega)$$

where the $\varepsilon_1(\omega)$ and $\varepsilon_2(\omega)$ are the real part of the function and the imaginary part, $\varepsilon_1(\omega)$ can derive from the imaginary part $\varepsilon_2(\omega)$ the dielectric function by Kramer–Kronig

can be expressed [40]. The imaginary part of the dielectric function can be expressed as

$$\varepsilon_2(\omega) = \frac{4\pi^2}{m^2 - \omega^2} \sum_{V,C} \int_{BZ} d^3k \frac{2}{2\pi} |e \cdot M_{cv}|^2 \times \delta[E_C \\ \times (k) - E_V(k) - \hbar\omega]$$

In addition, the absorption coefficient $I(\omega)$ was obtained by

$$I(\omega) = \sqrt{2}\omega \left[\sqrt{\varepsilon_1^2(\omega) - \varepsilon_2^2(\omega)} - \varepsilon_1(\omega) \right] 1/2$$

where the C is the conduction band, the V is valence band states, Ω is the unit-cell volume, m is the mass of free electrons, e is the charge of free electrons, and ω is the frequency of incident photons.

Results and Discussion
Stability
First, four 2D Sn_xP_y monolayers were considered to determine their energetic stabilities. Formation energy is an energy parameter in a thermodynamic system which is a key point to check the stability of the system. The relative stability of Sn_xP_y monolayers can be confirmed by computing the formation energy and is calculated as

$$E_{form} = (E_{total} - N_{Sn}E_{Sn} - N_P E_P)/(N_{Sn} + N_p)$$

where E is the energy of a compound or a constituent element at a specific pressure. N is the number of atoms in the unit cell. The negative formation energy of the calculated system indicates that the configuration is stable or metastable [41]. The calculated formation energies of Sn_xP_y monolayers are − 0.235, − 0.223, − 0.159, and − 0.016 eV/atom (shown in Table 1), respectively. According to its definition, a smaller value indicates higher stability. Obviously, P$\bar{6}$m2-SnP is the most stable of these four structures. More particularly, the high thermal stability of semiconductor materials is particularly important in the application of electronic devices. Here, the thermal stability of the Sn_xP_y monolayers examined by using ab initio molecular dynamics (AIMD) simulations. Based on the symmetries of the space groups, we

just calculate the stability of P$\bar{6}$m2-SnP for similar structures P$\bar{6}$m2-SnP and Pmc2$_1$-SnP$_2$ and Pmc2$_1$-SnP$_2$ for Pmc2$_1$-SnP$_2$and P$\bar{4}$2$_1$m-SnP$_2$ structures. Results indicate that the average value of the total energy of the structure remains almost unchanged, and the structure remains unchanged after 1 ps, 3 ps, and 5 ps, suggest that Sn_xP_y monolayers are thermally stable (in Figure S1). Then, we calculated phonon dispersion curves and have no imaginary vibrational frequencies implies that structures are dynamically stable (in Figure S1). Several methods have been reported in the literature to synthesize layered materials including micromechanical cleavage [2], epitaxial growth [42], chemical vapor deposition [43], and liquid exfoliation [44]. Some materials with the similar structure were successfully prepared experimentally. We have found some related reports that few layer GaSe nanosheets have been made into a high performance photodetector in the experiment [45]. In addition, the preparation, isolation, and rapid unambiguous characterization of large size ultrathin layers of MoS_2, GaS, and GaSe deposited onto SiO_2/Si substrates are reported [46].

As plotted in Fig. 1a, b, the structures of P$\bar{3}$m1-SnP exhibit a structure similar to the P$\bar{6}$m2-SnP hexagonal phase. The Pmc2$_1$-SnP$_2$ trigonal phase (Fig. 1c) exhibits that the x/y composition is further increased to 1/2. The material of a structure similar to P$\bar{4}$2$_1$m-SnP$_2$ was proved stable by theory calculation [47]. Also, a new study finds the structure of XY$_2$ (Fig. 1d) is an indirect bandgap semiconductor, and it might susceptible to electric field and stress. We believe that the material we predict will have a successful preparation in the future with the development of technology.

Electronic and Magnetic Properties
The computed band structures and partial density of states of Sn_xP_y monolayers are plotted in Fig. 2. As shown in Fig. 2a, the P6m2-SnP is an indirect semiconductor with a band gap of 1.19 eV. The valence band maximum (VBM) at $\Gamma \rightarrow K$ direction is contributed by the hybridized Sn-p and P-p orbitals, while the conduction band minimum (CBM) at K point derives from the hybridized Sn-s and P-p orbitals. P$\bar{3}$m1-SnP exhibits

Table 1 Lattice parameters and calculated formation energy of the Sn_xP_y monolayers

Sn_xP_y monolayers	Lattice parameters						Space group	Formation energy (eV/atom)
	a	b	c	Alpha	Beta	Gamma		
P$\bar{6}$m2-SnP	3.95	3.95	17.16	90	90	120	P$\bar{6}$m2	− 0.235
P$\bar{3}$m1-SnP	3.96	3.96	17.11	90	90	120	P$\bar{3}$m1	− 0.223
Pmc2$_1$-SnP$_2$	3.71	10.78	15.83	90	90	90	Pmc2$_1$	− 0.159
P$\bar{4}$2$_1$m-SnP$_2$	7.59	7.59	14.66	90	90	126.69	P$\bar{4}$2$_1$m	− 0.016
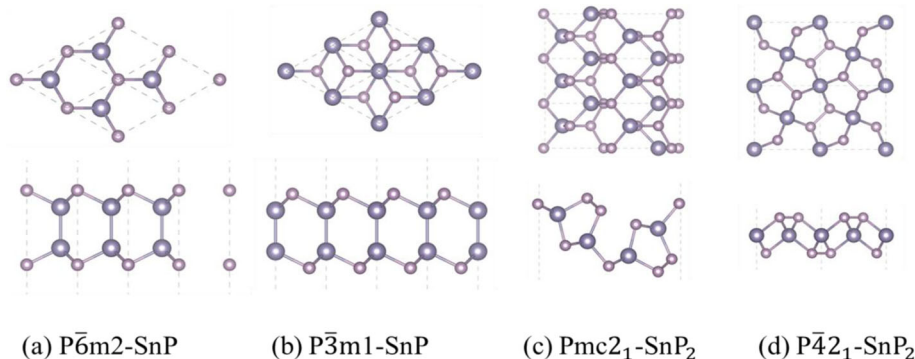
Fig. 1 Top and side views of the atomic structures of Sn_xP_y monolayers: **a** P$\bar{6}$m2-SnP, **b** P$\bar{3}$m1-SnP, **c** Pmc2_1-SnP$_2$, and **d** P$\bar{4}2_1$m-SnP$_2$; the Fermi level (horizontal dashed line) is shifted to 0 eV. The heavy pink spheres represent Sn atoms, and light pink spheres represent P atoms
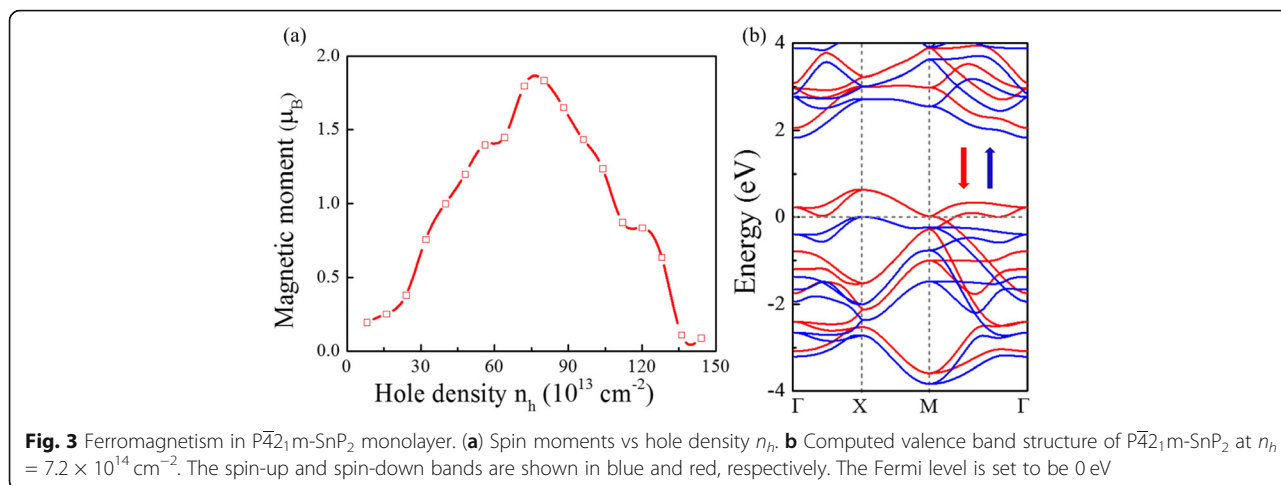
similar electronic band structures as the P$\bar{6}$m2-SnP counterpart but with a smaller band gap of 1.21 eV. The valence band dispersion of P$\bar{6}$m2-SnP and P$\bar{3}$m1-SnP near the Γ point and Fermi level (E_F) is quite flat, given the rather high density of states (DOS) and a van Hove singularity around the VBM. The Pmc2_1-SnP$_2$exhibits direct-like gap semiconducting character (E_g(direct) – E_g(indirect) = 6 meV) with a band gap of 0.72 eV (see Fig. 2c). Its VBM is mostly attributed to P-p orbitals, while its CBM is mainly contributed by P-p orbitals and Sn-s orbital. The P$\bar{4}2_1$m -SnP$_2$ is an indirect-gap semi-

conductor with an E_g of 1.79 eV, and the bands derive from is akin to Fig. 2c. More importantly, P$\bar{4}2_1$m-SnP$_2$monolayer has a similar condition compare with Fig. 2a, b, a flat-band dispersion character around the VBM also arises, resulting in very high DOS and a van Hove singularity.

According to Stoner criterion, spontaneous ferromagnetism occurs if the kinetic energy is smaller than the exchange splitting energy, which is if the DOS at E_F is high enough. Figure 2d shown the very high DOS around the VBM; the P$\bar{4}2_1$m-SnP$_2$ may satisfy the Stoner
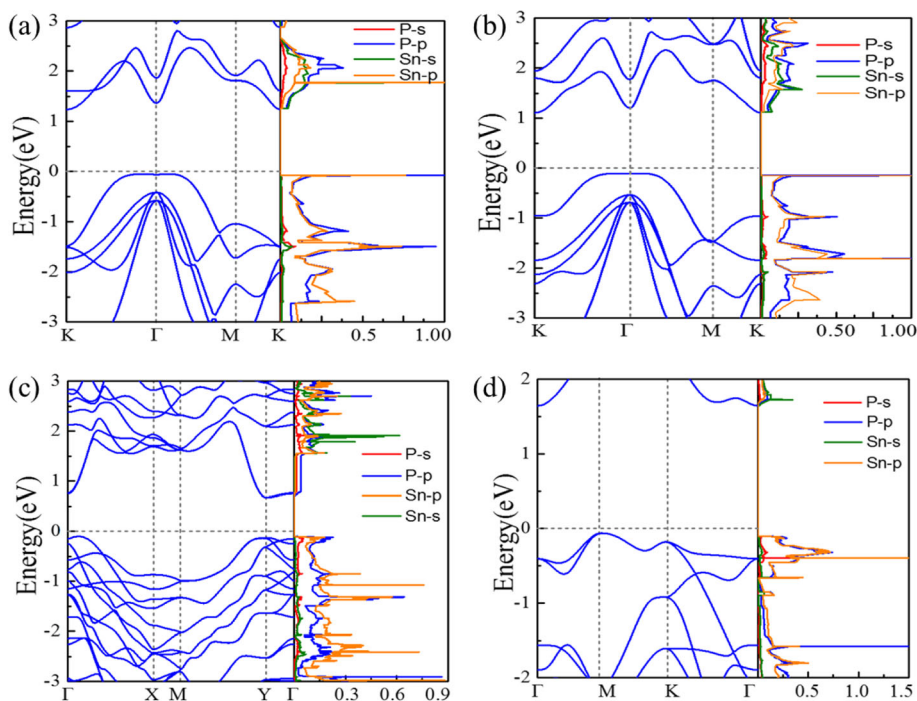
Fig. 2 Computed electronic band structures and partial density of states of the VBM and CBM of Sn_xP_y monolayers: **a** P$\bar{6}$m2-SnP, **b** P$\bar{3}$m1-SnP, **c** Pmc2_1-SnP$_2$, and **d** P$\bar{4}2_1$m-SnP$_2$

Fig. 3 Ferromagnetism in P$\bar{4}2_1$m-SnP$_2$ monolayer. (**a**) Spin moments vs hole density n_h. **b** Computed valence band structure of P$\bar{4}2_1$m-SnP$_2$ at n_h = 7.2 × 10^{14} cm^{-2}. The spin-up and spin-down bands are shown in blue and red, respectively. The Fermi level is set to be 0 eV
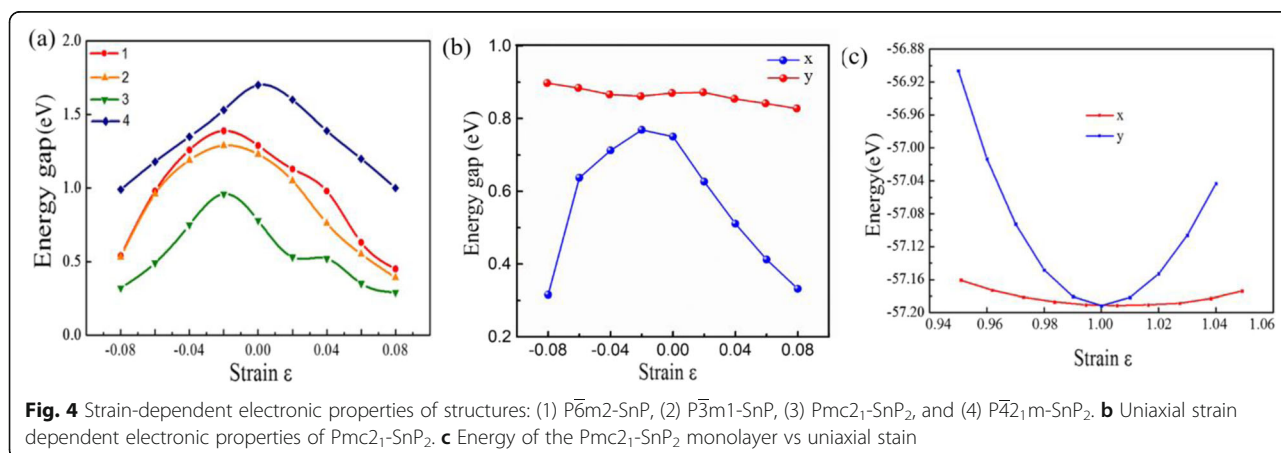
criterion if its E_F is shifted to a position with high DOS through hole doping. As shown in Fig. 3a, the hole doping can introduce magnetic moments at appropriate doping concentrations. As expected, the computation result suggests that the P$\bar{4}2_1$m-SnP$_2$ may be converted into a ferromagnetic ground state beyond the critical hole density. Among them, the hole density n_h can be expressed as $n_h = m_h/S_{cell}$, where S_{cell} and m_h are the area of the primitive cell and the number of holes introduced in the primitive cell. The injection of the hole into the monolayer P$\bar{4}2_1$m-SnP$_2$ indeed leads to ferromagnetism. The magnetic moment exhibits a steep peak-like relationship with the hole density. Because an appreciable spin moment is induced by hole doping in the system, the energy band structure around the Fermi level has changed greatly due to spin splitting. Particularly, the spin-polarized band structure (shown in Fig. 3b) of P$\bar{4}2_1$m-SnP$_2$ at 7.2 × 10^{14} cm^{-2} shows that the monolayer becomes a perfect half metal. So, we predict that the

stable FM state with half metallicity can be realized in the P$\bar{4}2_1$m-SnP$_2$ monolayer.

Elastic Anisotropy and Carrier Mobility of Monolayer

The strain effects on the electronic properties of the 2D monolayers Sn$_x$P$_y$ structures are also interesting. Figure 4a presents the energy gap variation under biaxial strain ε. The energy gap of Sn$_x$P$_y$ monolayers is markedly modulated according to some rules. For example, the energy gap of P$\bar{6}$m2-SnP decreases from 1.19 to 0.52 eV with the increasing tensile strain up to ε = 8%, first increasing from 1.12 to 1.36 eV for ε 2%, then decreasing from 1.36 to 0.51 eV. In addition, since the a and b of the lattice parameter of the Pmc2$_1$-SnP$_2$ structure are different, the changes of electronic properties are different along the x-axis and y-axis [48], as shown in Fig. 4b. It is obvious that when uniaxial strain is applied in different directions, the change in the x direction is different from the change in the y direction. Considering the range of energy gaps with the strain ε, the range of tunable band

Fig. 4 Strain-dependent electronic properties of structures: (1) P$\bar{6}$m2-SnP, (2) P$\bar{3}$m1-SnP, (3) Pmc2$_1$-SnP$_2$, and (4) P$\bar{4}2_1$m-SnP$_2$. **b** Uniaxial strain dependent electronic properties of Pmc2$_1$-SnP$_2$. **c** Energy of the Pmc2$_1$-SnP$_2$ monolayer vs uniaxial stain

Dou *et al. Nanoscale Research Letters* (2020) 15:155

Page 6 of 8

Table 2 Effective masses of electrons and holes for Pmc2$_1$-SnP$_2$

	Pmc2$_1$-SnP$_2$	
$|m^*_e|$	1.31 (K_a)	0.15 (k_b)
$|m^*_h|$	0.42 (k_a)	0.57 (k_b)

gap by in-plane strain almost covers the entire visible-light region based on the first-principles calculation.

Besides, we also investigated the effect of uniaxial stress, as shown in Fig. 4c. The in-plane stiffness C^{2D} (C^{2D} = $[\partial^2 E/\partial\delta^2]/S_0$, where S_0 is the area of 2D Pmc2$_1$-SnP$_2$ monolayer) can be obtained by fitting the parabola. Interestingly enough, the in-plane stiffness C^{2D} showing extremely obvious elastic anisotropy along a and b directions are calculated to be 12.1 and 105.6 N/m, respectively. Because the Pmc2$_1$-SnP$_2$ exhibits direct-like gap semiconducting character, the effective masses (m^* = $\hbar^2(\partial^2 E/\partial K^2)^{-1}$) of electrons ($m_e$ is $|m^*_e|$) and holes (m_h is $|m^*_h|$) associated with the (quasi) direct semiconducting Pmc2$_1$-SnP$_2$ monolayer are also computed. The effective masses are listed (Table 2). Most interesting is the effective mass of electrons in the k_b direction (0.15 me) is much smaller than that in the k_a direction (1.31 me), indicating the easy drift of electrons in the k_b direction. There is another important parameter is DP constant E_1 (E_1 = dE_{edge}/dδ) for electrons along a and b directions is calculated to be 5.36 and 11.57 eV, respectively. Surprisingly, the calculated carrier can be achieved ~ 800 cm^{2}V^{-1} s^{-1} in the k_b direction. As a comparison, the carrier mobility of the MoS$_2$ monolayer is ~ 200 cm^{2}V^{-1} s^{-1} in experiments [8]. However, the carrier mobility is just about ~ 8 cm^{2}V^{-1} s^{-1} in the k_a direction. Therefore, the high carrier mobility found in this study is of great significance for the study of electron transport.

Optical Property

The photoelectric properties of photoelectronic materials are characterized by dielectric function, photoconductivity, and absorption coefficient. The imaginary parts of the dielectric function are shown in Fig. 5a. Note that Pmc2$_1$-SnP$_2$ monolayer shows absorption starting at ~ 0.70 eV, and there appear three main absorption peaks at ~ 0.9, ~ 3.2, and ~ 4.0 eV. As illustrated in Fig. 5b, it shows the absorbance in all three directions in the visible range and ultraviolet range for monolayer Pmc2$_1$-SnP$_2$. So, Pmc2$_1$-SnP$_2$ monolayer materials could be used for atomically thin solar-blind photodetectors for, e.g., efficient detection of flames.

Conclusions

In conclusion, based on the PSO algorithms combined with first-principles calculations, we have identified several 2D Sn$_x$P$_y$ monolayers with the ratios of x/y = 1:1 and 1:2. Surprisingly, these novel monolayers also possess peculiar electronic and magnetic properties: the monolayer of P$\overline{4}2_1$m-SnP$_2$ structure with unique valence band structure can go from nonmagnetic to ferromagnetic by the hole doping because of the "Stoner criterion"; the Pmc2$_1$-SnP$_2$ structure is a direct-like gap semiconductor with in-plane elastic anisotropy is found to possess high electron mobility as high as 800 cm^{2}V^{-1} s^{-1} along the k_b direction, which is much higher than that of MoS$_2$ (~ 200 cm^{2}V^{-1} s^{-1}). The optical absorption peak of the material is in the ultraviolet region. These
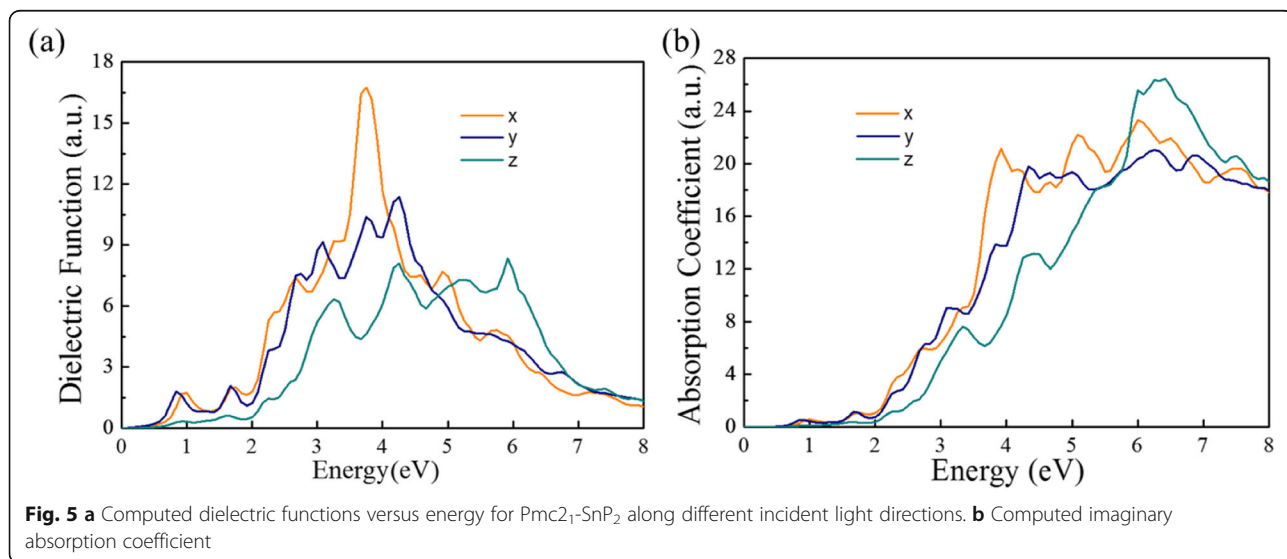
Fig. 5 a Computed dielectric functions versus energy for Pmc2$_1$-SnP$_2$ along different incident light directions. **b** Computed imaginary absorption coefficient

Dou *et al. Nanoscale Research Letters* (2020) 15:155

Page 7 of 8

discoveries expand the potential applications of the emerging field of 2D Sn_xP_y structures in nanoelectronics. These desirable properties of the multifunctional Sn_xP_y monolayers provide promising great applications in electronics and optoelectronics.

Supplementary information

Supplementary information accompanies this paper at https://doi.org/10.1186/s11671-020-03383-0.

> **Additional file 1: Figure S1.** The total energy and kinetic energy versus the simulation steps; final equilibrium structures (inset) at T=300 K structures of Sn_xP_y monolayers: (a) P6◻m2-SnP, (b) Pmc2₁-SnP₂; the Fermi level (horizontal dashed line) is shifted to 0 eV.

Authors' Contributions
P-JW and C-WZ conceived the idea and designed the calculated model. Y-MD carried out the calculations and data analysis. PL performed the analysis method of optical properties. All authors read and approved the final manuscript.

Availability of Data and Materials
They are all in the main text and figures.

Competing Interests
The authors declare that they have no competing interests

References

1. Jariwala D, Sangwan VK, Lauhon LJ, Marks TJ, Hersam MC (2014) Emerging device applications for semiconducting two-dimensional transition metal dichalcogenides. ACS Nano 82:1102–1120
2. Novoselov KS, Geim AK, Morozov SV, Jiang D, Zhang Y, Dubonos SV, Grigorieva IV, Firsov AA (2004) Electric field effect in atomically thin carbon films. Science 306(5696):666–669
3. Novoselov KS, Geim AK, Morozov SV, Jiang D, Katsnelson MI, Grigorieva IV, Dubonos SV, Firsov AA (2005) Two-dimensional gas of massless Dirac fermions in graphene. Nature 438:197–200
4. Novoselov KS, McCann E, Morozov SV, Fal'ko VI, Katsnelson MI, Zeitler U, Jiang D, Schedin F, Geim AK (2006) Unconventional quantum Hall effect and Berry's phase of 2π in bilayer graphene. Nat Phys 2:177–180
5. Zhang Y, Tan Y-W, Stormer HL, Kim P (2005) Experimental observation of the quantum Hall effect and Berry's phase in graphene. Nature 438:201–204
6. Wang Z, Zhuang H, Yu S et al (2019) An ultraflexible and stretchable aptameric graphene nanosensor for biomarker detection and monitoring. Adv Funct Mater 1905202
7. Pacilé, D.; Meyer, J. C.; Girit, Ç. Ö .; Zettl, A. The two-dimensional phase of boron nitride: few-atomic-layer sheets and suspended membranes. Appl Phys Lett, 2008, 92, 133107.
8. Radisavljevic B, Radenovic A, Brivio J, Giacometti V, Kis A (2011) Single-layer MoS2 transistors. Nat Nanotechnol 6:147–150
9. Wang QH, Kalantar-Zadeh K, Kis A, Coleman JN, Strano MS (2012) Electronics and optoelectronics of two-dimensional transition metal dichalcogenides. Nat Nanotechnol 7:699–712
10. Ramakrishna Matte HSS, Gomathi A, Manna AK, Late DJ, Datta R, Pati SK, Rao CNR (2010) MoS2 and WS2 analogues of graphene. Angew Chem Int Ed 49:4059–4062
11. Feng J, Peng L, Wu C, Sun X, Hu S, Lin C, Dai J, Yang J, Xie Y (2012) Giant moisture responsiveness of VS2 ultrathin nanosheets for novel touchless positioning interface. Adv Mater 24:1969–1974
12. Jeon PJ, Min S-W, Kim JS, Raza SRA, Choi K, Lee HS, Lee YT, Hwang DK, Choi HJ, Im S (2015) Enhanced device performances of WSe2-MoS2 van der Waals junction p-n diode by fluoropolymer encapsulation. J Mater Chem C 3:2751–2758
13. Fang H, Chuang S, Chang TC, Takei K, Takahashi T, Javey A (2012) High-performance single layered WSe2 p-FETs with chemically doped contacts. Nano Lett 12:3788–3792
14. Dai J, Zeng XC (2015) Titanium trisulfide monolayer: theoretical prediction of a new direct-gap semiconductor with high and anisotropic carrier mobility. Angew Chem Int Ed 54:7572–7576
15. Li M, Dai J, Zeng XC (2015) Tuning the electronic properties of transition-metal trichalcogenides via tensile strain. Nanoscale 7:15385–15391
16. Dávila ME, Xian L, Cahangirov S, Rubio A, Lay GL (2014) Germanene: a novel two-dimensional germanium allotrope akin to graphene and silicone. New J Phys 16:095002
17. Liu H, Neal AT, Zhu Z, Luo Z, Xu X, Tománek D, Ye PD (2014) Phosphorene: an unexplored 2D semiconductor with a high hole mobility. ACS Nano 8: 4033–4041
18. Koenig SP, Doganov RA, Schmidt H, Castro Neto AH, ÖZyilmaz B (2014) Electric field effect in ultrathin black phosphorus. Appl Phys Lett 104:103106
19. Li L, Yu Y, Ye GJ, Ge Q, Ou X, Wu H, Feng D, Chen XH, Zhang Y (2014) Black phosphorus field-effect transistors. Nat Nanotechnol 9:372–377
20. Zhang S, Yan Z, Li Y, Chen Z, Zeng H (2015) Atomically thin arsenene and antimonene: semimetal–semiconductor and indirect–direct band-gap transitions. Angew Chem Int Ed 54:3112–3115
21. Li H, Duan X, Wu X, Zhuang X, Zhou H, Zhang Q, Zhu X, Hu W, Ren P, Guo P, Ma L, Fan X, Wang X, Xu J, Pan A, Duan X (2014) Growth of alloy MoS2xSe2(1−x) nanosheets with fully tunable chemical compositions and optical properties. J Am Chem Soc 136:3756–3759
22. Duan X, Wang C, Fan Z, Hao G, Kou L, Halim U, Li H, Wu X, Wang Y, Jiang J, Pan A, Huang Y, Yu R, Duan X (2016) Synthesis of WS2xSe2−2x alloy nanosheets with composition-tunable electronic properties. Nano Lett 16: 264–269
23. Li P, Zhou R, Zeng XC (2014) The search for the most stable structures of silicon–carbon monolayer compounds. Nanoscale 6:11685–11691
24. Luo X, Yang J, Liu H, Wu X, Wang Y, Ma Y, Wei S-H, Gong X, Xiang H (2011) Predicting two-dimensional boron–carbon compounds by the global optimization method. J Am Chem Soc 133:16285–16290
25. Dai J, Zhao Y, Wu X, Yang J, Zeng XC (2013) Exploration of structures of two-dimensional boron–silicon compounds with sp 2 silicon. J Phys Chem Lett 4:561–567
26. Wang Y, Lv J, Zhu L, Ma Y (2010) Crystal structure prediction via particle-swarm optimization. Phys Rev B: Condens Matter Mater Phys 82:094116
27. Houssa MB, van den Broek B, Scalise E (2013) An electric field tunable energy band gap at silicene/(0001) ZnS interfaces. Phys Chem Chem Phys 15:3702–3705
28. Perdew JP, Burke K, Ernzerhof M (1997) Erratum: Generalized gradient approximation made simple. Phys Rev Lett 78:3865
29. Kresse G, Furthmüller J (1996) Efficient iterative schemes for ab initio total-energy calculations using a plane-wave basis set. Phys Rev B Condens Matter 54:11169–11186
30. Kresse G, Hafner J (1994) Ab initio molecular-dynamics simulation of the liquid-metal–amorphous-semiconductor transition in germanium. Phys Rev B 49:14251
31. Houssa M, Scalise E, Pourtois G, Afanas'Ev VV, Stesmans A (2013) An electric field tunable energy band gap at silicene/(0001) ZnS interfaces. Phys Chem Chem Phys 15:3702–3705
32. Perdew JP, Wang Y (1992) Pair-distribution function and its coupling-constant average for the spin-polarized electron gas. Phy Rev B: Condensed Matter 46:12947
33. Kresse G, Joubert D (1999) From ultrasoft pseudopotentials to the projector augmented-wave method. Phys.Rev.B 59:1758–1775
34. Perdew JP, Ruzsinszky A, Csonka GI (2008) Erratum: Restoring the density-gradient expansion for exchange in dolids and surfaces. Phys Rev Lett 100: 136406
35. Perdew JP, Burke K, Ernzerhof M (1996) Erratum: Generalized gradient approximation made simple. Phys Rev Lett 77:3865
36. Martyna GJ, Klein ML, Tuckerman M (1992) Nosé–Hoover chains: the canonical ensemble via continuous dynamics. J Chem Phys 97:2635–2643
37. Bardeen J, Shockley W (1950) Deformation potentials and mobilities in non-polar crystals. Phys Rev 80:72

38. Price PJ (1981) Two-dimensional electron transport in semiconductor layers. I. Phonon Scattering. Ann Phys 133:217–239
39. Xi J, Long M, Tang L, Wang D, Shuai ZG (2012) First-principles prediction of charge mobility in carbon and organic nanomaterials. Nanoscale 4:4348–4369
40. Gajdoš M, Hummer K, Kresse G (2006) Linear optical properties in the projector-augmented wave methodology. Phys Rev B 20:045112
41. Li Q, Zhou D, Zheng W (2013) Global structural optimization of tungsten borides. Phys Rev Lett 110:136403
42. Berger C, Song Z, Li T, Li X, Ogbazghi AY, Feng R, Dai Z, Marchenkov AN, Conrad EH, First PN, de Heer WA (2004) United atom force field for alkanes in nanoporous materials. J Phys Chem B 108(33):12301–12313
43. Rosei R, Modesti S, Sette F, Quaresima C, Savoia A, Perfetti P (1984) Electronic structure of carbidic and graphitic carbon on Ni(111). Phys Rev B 29(6):3416–3422
44. Coleman JN, Lotya M, Neill AO, Bergin SD, King PJ, Khan U, Young K, Gaucher A, De S, Smith RJ, Shvets IV, Arora SK, Stanton G, Kim H, Lee K, Kim GT, Duesberg GS, Hallam T, Boland JJ, Wang JJ, Donegan JF, Grunlan JC, Moriarty G, Shmeliov A, Nicholls RJ, Perkins JM, Grieveson EM, Theuwissen K, McComb DW, Nellist PD, Nicolosi V (2011) Tunable dielectric properties of transition metal dichalcogenides. ACS Nano 5(7):5903–5908
45. Hu PA, Wen Z, Wang L (2012) Synthesis of few-layer GaSe nanosheets for high performance photodetectors. ACS Nano 6(7):5988–5994
46. Late DJ, Liu B, Matte HSSR (2012) Rapid characterization of ultrathin layers of chalcogenides on SiO2/Si substrates. Adv Funct Mater 22(9):1894–1905
47. Aierken Y, Leenaerts O, Peeters FM (2016) A first-principles study of stable few-layer penta-silicene. Phys Chem Chem Phys 18(27):18486–18492
48. Fan ZQ, Jiang XW, Wei ZM, Luo JW, Li SS (2017) Tunable electronic structures of GeSe nanosheets and nanoribbons. J Phys Chem C 121(26):14373–14379

Publisher's Note